Available online at www.sciencedirect.com
ScienceDirect
Earth and Planetary Science Letters 259 (2007) 239–255
EPSL
www.elsevier.com/locate/epsl

Axial crustal structure of the Lau back-arc basin from velocity modeling of multichannel seismic data

Allison M. Jacobs *, Alistair J. Harding, Graham M. Kent

Scripps Institution of Oceanography, University of California, San Diego, La Jolla, CA 92093-0225, USA

Received 8 September 2006; received in revised form 6 April 2007; accepted 6 April 2007
Available online 19 April 2007
Editor: R.D. van der Hilst

Abstract

Located west of the Tonga trench, the Lau back-arc basin is a prime environment for studying the interplay between oceanic spreading systems and an active subduction zone. Within the basin lie two complementary, intermediate-rate spreading systems, the Central Lau Spreading Center (CLSC) and the Eastern Lau Spreading Center/Valu Fa Ridge (ELSC/VFR), that are positioned 170 to 40 km away from the active volcanic arc, respectively. Multichannel seismic (MCS) images of both systems reveal systematic variations in axial crustal structure primarily related to the proximity of the volcanic arc, but also related to spreading rate, morphology, and petrology. Upper crustal refraction data selected from the along-axis seismic lines collected during the 1999 MCS survey were modeled in both the time-versus-range (t–x) and intercept time-versus-slowness (τ–p) domains to provide validation and detail to the seismic reflection observations. The results show that as both the proximity to the arc and the spreading rate decrease southward: 1) seismic layer 2A thickens by 0.6 km between the CLSC and VFR, from 0.4 km to 1.0 km, 2) the average depth of the axial magma chamber (AMC) increases from 1.5 km at the CLSC to 2.8 km at the southern VFR, excluding the northern section of the ELSC that shows no continuous AMC reflector, but does show an isolated melt sill, 3) the upper crustal basement velocity decreases from 2.1 km/s at the CLSC to 1.8 km/s at the VFR, and 4) the velocities of both layer 2A and 2B decrease between the CLSC and northern VFR from 3.2 to 2.5 km/s and 5.0 to 3.9 km/s, respectively. Along with a broad axial high morphology, these features of the CLSC — thinner layer 2A, shallower AMC, and faster crustal velocities — correlate best with the fast spreading East Pacific Rise and intermediate spreading Juan de Fuca Ridge. Conversely, the structural characteristics of the central ELSC/VFR have no known counterpart in the global mid-ocean ridge system. We attribute this primarily to the volatile concentration in the magmas coming from the Tonga subduction zone.
Published by Elsevier B.V.

Keywords: back-arc ridges; oceanic crustal structure; multichannel seismic survey; velocity modeling; Lau basin

1. Introduction

The crustal structure of mid-ocean ridges has been extensively studied by seismic methods for a number of decades (e.g., White, 1979). More modern surveys have utilized higher resolution multichannel seismic (MCS) techniques to elucidate the finer structure of the upper crust, both horizontally and vertically. However, the majority of these surveys have been conducted along better known fast- and slow-spreading ridges, such as the East Pacific Rise (EPR) (e.g., Harding et al., 1993; Kent et al., 1994) and Mid-Atlantic Ridge (MAR) (e.g., Detrick et al., 1995; Singh et al., 2006), leaving a significant void of

* Corresponding author. Tel.: +1 858 534 2562; fax: +1 858 534 6354.
E-mail address: amjacobs@ucsd.edu (A.M. Jacobs).

0012-821X/$ - see front matter. Published by Elsevier B.V.
doi:10.1016/j.epsl.2007.04.021

information on intermediate-spreading ridges. Modeling suggests that for this class of ridges, the axial structure exhibits a greater sensitivity to variables such as magma supply (Morgan and Chen, 1993; Chen and Lin, 2004). To further examine this, as well as other characteristics, MCS surveys were recently carried out along the Juan de Fuca Ridge (JdFR) (Canales et al., 2005; Nedimović et al., 2005; Van Ark et al., 2007), the Galapagos Spreading Center (Canales et al., 2002; Blacic et al., 2004), and the Southeast Indian Ridge (Baran et al., 2005), all spreading at intermediate rates. This study of the along-axis crustal structure of two intermediate-rate spreading systems in the Lau back-arc basin provides additional information about these lesser studied ridges, while also taking advantage of the Lau basin's back-arc environment to begin investigating the effects on seismic structure of the interplay between spreading centers and active subduction zones.

The Lau basin was one of the first areas for which a strong axial magma chamber (AMC) reflector was recognized in MCS data. In 1982, two MCS profiles crossing the central Valu Fa Ridge (VFR) revealed a strong reflector about 3.5 km below the ridge axis (Morton and Sleep, 1985). A second, more comprehensive survey of the VFR was conducted between 22°30'S and just north of the 22°10'S overlapping spreading center using a shorter, 4-channel streamer, as well as sonobuoys to gain wide-angle seismic data (Collier and Sinha, 1990; Collier and Sinha, 1992). This survey imaged an intermittent shallow reflector ~1 km below the seafloor and a nearly continuous AMC reflector approximately 3.2 km below the seafloor along the VFR. In addition, modeling predicted axial velocities increasing from ~1.8 km/s at the basement to ~5.3 km/s just above the AMC. The reflector depths and crustal velocities are respectively deeper and slower than any found along EPR (e.g., Harding et al., 1989; Vera et al., 1990; Kappus et al., 1995; Tolstoy et al., 1997) or MAR (e.g., Hussenoeder et al., 2002a), and thus implied a strong influence from an additional mechanism on the crustal structure of the VFR.

This third MCS survey of the Lau basin (Fig. 1) imaged both the Central Lau Spreading Center (CLSC) and Eastern Lau Spreading Center/Valu Fa Ridge (ELSC/VFR), extending the MCS coverage to a regional scale. The strong AMC reflector was again visible along the VFR axis, and by extending the study area north, we also observed how the along-axis crustal structure changes between the subduction zone-influenced VFR and the more "typical" CLSC that lies beyond the subduction zone influence (Pearce et al., 1995). As a Ridge 2000 integrated study site, our analysis of the Lau basin upper crustal structure can be combined with other measurements (e.g., morphology, petrology, seismicity, and hydrothermal activity) to help uncover cross-disciplinary processes that exist when oceanic spreading occurs in the presence of an active subduction zone.

2. Location, formation, and geologic characteristics of the Lau basin

The Lau basin is a wedge-shaped back-arc basin located in the southwest Pacific Ocean, just west of the Tonga trench. In the southern half of the basin lie two complementary, intermediate-rate spreading systems, the CLSC and the ELSC/VFR (Fig. 1). While the early tectonic history of the basin remains poorly understood, primarily due to the limited number of clear magnetic anomalies pre-dating organized seafloor spreading (Taylor et al., 1996), ODP Leg 135 established that the basin began opening roughly 6 Ma. The opening was initially driven by crustal extension and rifting apart of the existing island arc, and followed by the early stages of magmatic intrusion (Hawkins et al., 1994; Hawkins, 1995). Remnants of the rifted arc serve as geographic bounds for the current basin with the Lau Ridge to the west and the Tonga Ridge to the east (Parson and Wright, 1996); the present volcanic arc, the Tofua Volcanic Arc, is inboard of the Tonga arc on the eastern boundary of the basin. Between about 4–2 Ma, the tip of crustal accretion that had developed in the northern part of the basin, migrated southward from ~16.5° S to ~20° S (Parson and Hawkins, 1994). This initial ELSC propagated southward into older crust, preferentially rifting into areas near the active volcanic arc and generating the wake-like surface features, or pseudofaults, marked in Fig. 1. At ~2 Ma, the spreading system underwent a mild clockwise rotation, resulting in the formation of the CLSC, the Peggy Ridge transform fault, and an extensional transform zone between the two (Fig. 1) (Taylor et al., 1996). Subsequently, both spreading systems have continued to propagate southward with the CLSC beginning to overtake the northern part of the ELSC as the dominant spreading center in the central Lau basin (Parson and Hawkins, 1994; Parson and Wright, 1996).

The present CLSC and ELSC/VFR spreading systems are often divided into four sections based on morphology to expose the along-axis variability. The CLSC shows a continuous broad axial high, while the three major southern sections transition from an axial trough along the northern ELSC (nELSC), to a rounded high along the central ELSC (cELSC), to a steep, blade-like high along the VFR (Figs. 1 and 2 (top panel), Table 1) (Wiedicke and Collier, 1993; Martinez and Taylor, 2002).

While not considered a distinct section for this analysis, the short, 26 km segment between the nELSC

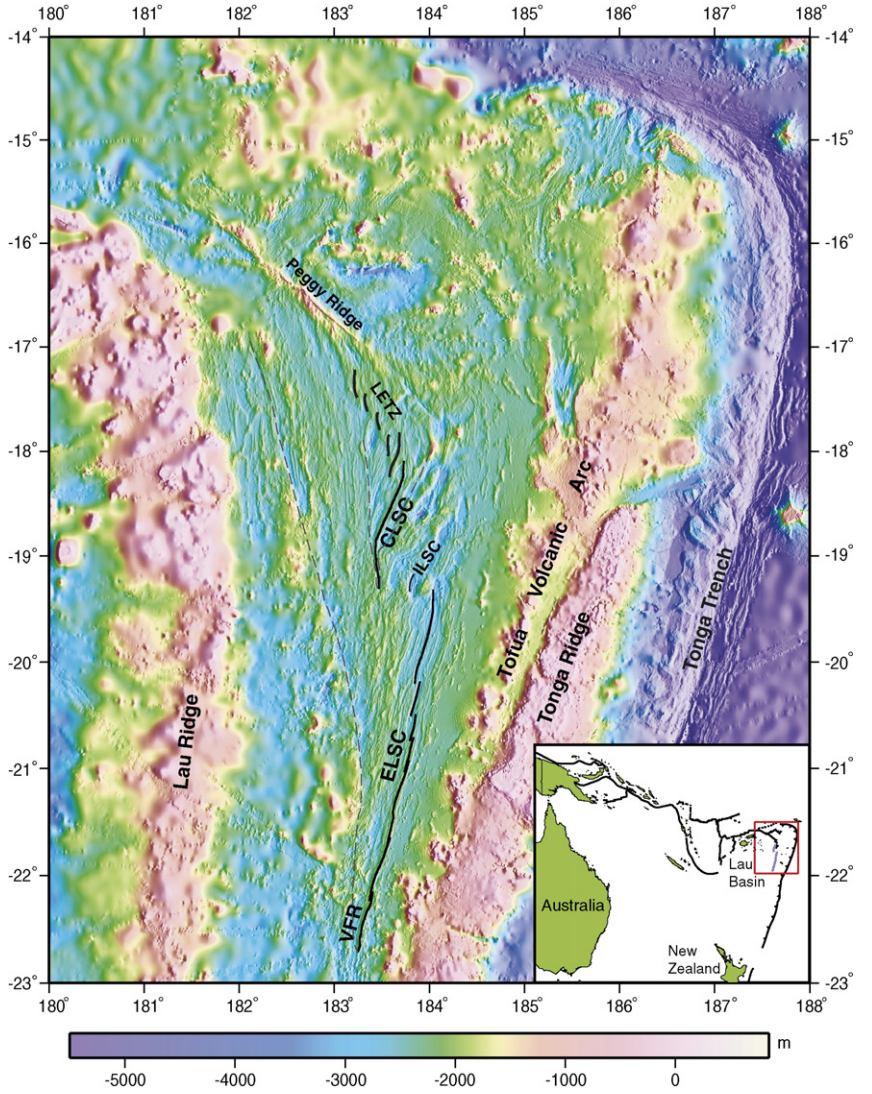

Fig. 1. Map of the Lau basin. Marked features within the basin are the Peggy Ridge, Lau Extensional Transitional Zone (LETZ), Central Lau Spreading Center (CLSC), Intra-Lau Spreading Center (ILSC), Eastern Lau Spreading Center (ELSC), and Valu Fa Ridge (VFR). Dashed black lines mark the psuedofaults. Red box in inset map shows the location of the Lau basin in a regional context. Bathymetry from Martinez et al. (2006) and Taylor et al. (1996).

and cELCS exhibits a fairly rapid change between the axial trough and axial high morphology of the nELSC and cELSC, respectively.

Concurrent with the morphologic variability, the four sections also exhibit gradual changes in characteristics such as distance from the volcanic arc, spreading rate, and petrology (Table 1). Offset an average of ~170 km west of the arc, the CLSC is spreading at about 90 mm/yr (Martinez and Taylor, 2002; Zellmer and Taylor, 2001) and rock samples show an N-MORB (mid-ocean ridge basalt) signature similar to many other mid-ocean ridges (Pearce et al., 1995). Beginning at the northern end of the ELSC, the ELSC/VFR shows a steady southward decrease in both distance from the arc and spreading rate, at 110–45 km and 95–40 mm/yr, respectively. Additionally, the chemical compositions of the magmas change from being MORB-like along the nELSC to predominately andesitic, or arc-like, along VFR section (Pearce et al., 1995). This study will show how these changes, both sharp and gradual, coincide with the structural features of the upper crust.

3. Variability of oceanic crustal structure

At intermediate- and fast-spreading mid-ocean ridges, upper oceanic crust exhibits a fairly consistent along-axis seismic structure. Typically, a thin (<500 m) layer overlays a thicker (~1500 m) layer that is underlain by an

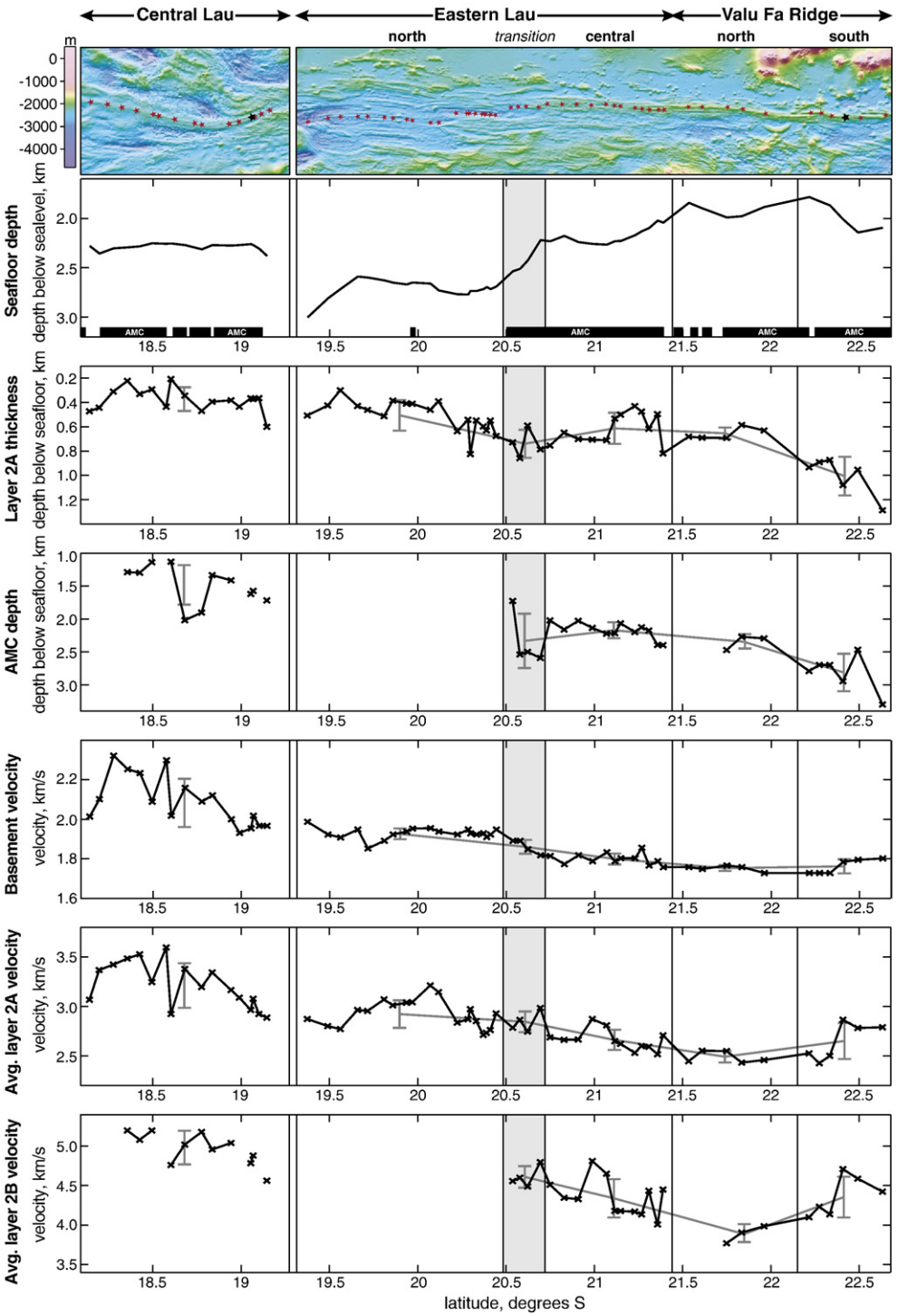

Fig. 2. Along-axis variations in bathymetry and crustal structure. Spreading centers are divided into four major sections based on similar features-CLSC, northern ELSC, central ELSC, and VFR. The VFR is additionally divided into north and south regions at the 22°10'S overlapping spreading center. Top panel shows axial bathymetry from Martinez et al. (2006) and Taylor et al. (1996) with stars denoting location of each of the 63 models used in this analysis; black stars denote locations of examples shown in Figs. 3 and 4, and Supplementary Figs. 1 and 2. The second panel highlights the seafloor depths (values from Martinez et al., 2006 and Taylor et al., 1996), as well as the location of an AMC event in our data. In the subsequent panels, each 'x' denotes the appropriate value of each model. Gray error bars representing one standard deviation above and below the mean value for each section. The gray region identifies the transitional segment.

Table 1
Physical characteristics of the major along-axis sections of the Lau basin spreading systems

Characteristics	CLSC	Northern ELSC	Central ELSC	VFR	
General					
End coordinates of sections	18.1° S, 176.3° W	19.3° S, 176.0° W	20.7° S, 176.2° W	21.4° S, 176.4° W	
(north/south)	19.3° S, 176.5° W	20.5° S, 176.2° W	21.2° S, 176.3° W	22.7° S, 176.7° W	
Spreading rate	85–90 mm/yr	95–77 mm/yr	73–63 mm/yr	63–40 mm/yr	
Distance from arc	185–160 km	110–77 km	71–63 km	63–45 km	
Axial morphology	Broad high	Rifted trough	Rounded high	Blade-like high	
Avg. seafloor depth	2.29 km	2.71 km	2.17 km	1.94 km	
Petrology	MORB-like signature	MORB-like with slight signature of depleted basalts	Strongly-depleted basalts to basaltic andesites	Strong arc signature: basaltic andesites to rhyodacites	
Crustal structure				*North*	*South*
Avg. layer 2A thickness	0.38 km	0.51 km	0.62 km	0.66 km	1.00 km
Avg. AMC depth	1.46 km	–	2.18 km	2.34 km	2.82 km
Avg. basement velocity	2.09 km/s	1.93 km/s	1.80 km/s	1.75 km/s	1.76 km/s
Avg. layer 2A velocity	3.26 km/s	3.00 km/s	2.68 km/s	2.51 km/s	2.67 km/s
Avg. layer 2B velocity	4.98 km/s	–	4.34 km/s	3.93 km/s	4.36 km/s

Spreading rates, arc-to-spreading center distances, and seafloor depths from Pearce et al. (1995), Taylor et al. (1996). Average depth and velocity values for the sections (and subsections of the VFR) are results of this study. For reference, layer 2A is defined as extending from the seafloor to the depth at which the velocity gradient noticeably decreases (see Figs. 4 and 5 and Supplementary Fig. 3). No AMC depth and layer 2B velocities are listed for the nELSC due to the lack of AMC reflections along this line.

axial magma chamber reflection. Commonly referred to as seismic layers 2A and 2B, the velocities for the topmost portion of these layers tend to have velocities around 2.5 km/s and 5.5 km/s, respectively, with a high velocity gradient of 1–3 s^{-1} in the transition zone between the layers (Vera et al., 1990; Harding et al., 1993; Carlson, 1998). When looking at crust in the vicinity of a spreading axis, the layer 2A/2B boundary is frequently considered to mark, or closely track, the transition from pillow basalts to sheeted basaltic dike; however, recent work by Christeson et al. (2007) show this relationship to be imperfect at intermediate spreading rates. Along the axis of the fast-spreading EPR, in particular, the thickness and velocity values for these two layers can be mapped for vast distances with only minimal deviations, mimicking the subdued variability of the axial morphology (e.g., Harding et al., 1993; Kent et al., 1994; Hooft et al., 1996). Conversely, in a back-arc spreading regime such as the Lau basin, we find that the seismic structure can show rapid and wide variations in both thickness and velocity of the upper crustal layers over a much shorter distance, yet still correlates with variations in axial morphology and other seafloor characteristics (Table 1, Fig. 2).

4. Data acquisition

The Lau basin 1999 MCS reflection experiment was a reconnaissance-style survey that utilized the *R/V Maurice Ewing*'s 480-channel, 6-km-long streamer to collect upper crustal seismic data along the CLSC and ELSC/VFR. Guided by bathymetry from Taylor et al. (1996), the experiment design included seismic profiles along the entire lengths of the spreading centers, 25 cross-axis lines, and a number of ridge-parallel and ridge-oblique off-axis lines. Due to the long length of the streamer, we also collected refraction data down to the depth of ~3.2 km below the seafloor along every axial profile.

The seismic data were sorted into common-mid-point (CMP) gathers with a 6.25 m bin spacing and all lines were processed to create seismic sections spanning the length of each profile line (small portions displayed in Fig. 3). Reflections from the layer 2A/2B interface are visible along all axial profiles, while the reflections from the AMC are visible along most of the axes, the exceptions occurring along the axial trough of the northern ELSC, towards the propagating tips of both ridges, and near the transitional segment (Fig. 2). Areas where the seafloor and both major subsurface reflectors appeared flat over a distance of 300 m or more were identified as potential locations for velocity analysis because we could assume an approximate one-dimensional structure. Each constant offset stack, or "supergather", in these areas combined either 48 or 96 adjacent CMP gathers, equating to a reflection point spread of 300 m or 600 m, respectively (Diebold and Stoffa, 1981). Given the 12.5 m channel spacing and 37.5 m shot spacing, these numbers were chosen such that the supergathers had 8 to 16 fold data over the entire ~200–

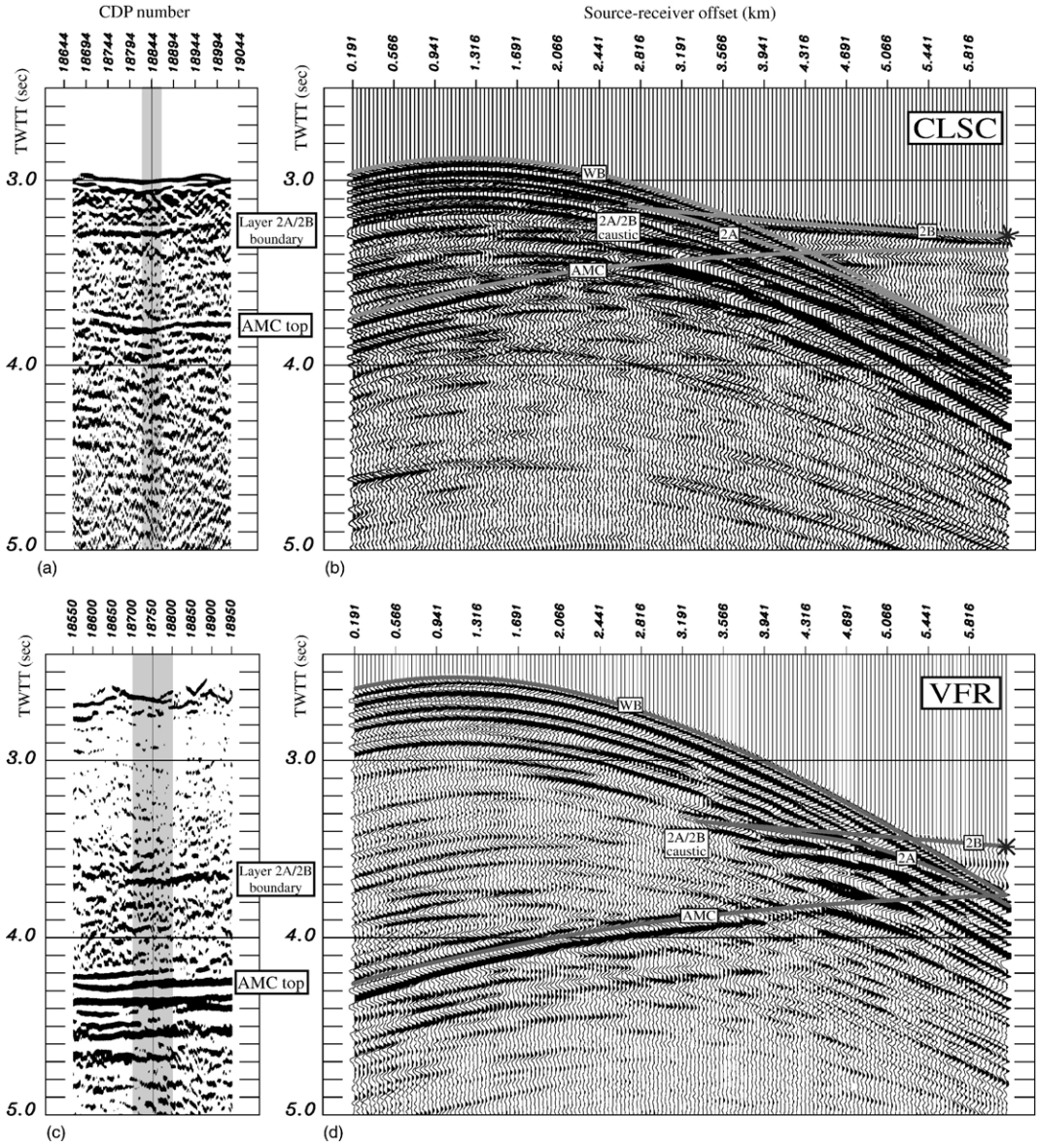

Fig. 3. Local along-axis stack from the (a) CLSC (~19.0°S) and (c) VFR (~22.3°S). Gray stripe shows the range of traces stacked to form the respective *t–x* supergathers in (b) and (d). Supergathers are overlain with travel-time curve (gray lines) generated from velocity–depth models in Fig. 4. Due to the relatively shallow AMC of the CLSC, the 6-km streamer recorded reflections off the water bottom, layer 2A/2B interface, and AMC, as well as refractions from a substantial portion of layer 2B. While nearly the same total depth below the seafloor is sampled along both the CLSC and VFR, nearly all layer 2B information for the VFR is estimated from modeling the AMC reflection event. This is due to the relatively deep AMC and thick layer 2A causing the streamer to record only limited refractions from layer 2B. The dark gray stars in (b) and (d) correspond to the respective dark gray stars on the velocity models (Fig. 4) that show the maximum depth at which rays sample layer 2B.

6200 m offset range of the data. The fold value permitted each supergather to attain a moderate signal-to-noise improvement, highlighting the stronger arrivals for analysis. Spaced at roughly 7.7 km increments along the axial profiles, a total of 63 supergathers (Fig. 2) provided a diverse dataset for examining the along-axis variability of the Lau basin upper crustal structure.

5. Methods and results

5.1. Velocity modeling

Preliminary processing of the Lau basin data revealed significant structural variability in the upper crust. As a result, we chose to quantify the first order variations by

simultaneously and interactively fitting travel time curves to 63 supergathers displayed in both time-versus-range (t–x) and intercept-versus-slowness (τ–p) transformed supergathers. For each supergather, we started with a 10-node velocity–depth model and the associated t–x and τ–p travel-time curves. The model was then adjusted interactively until a satisfactory travel-time fit to all visible P-wave events was found.

Both the t–x and τ–p transformed data were incorporated into this analysis as it is much easier to accurately estimate the slowness, and hence the velocity, of the basement and top of layer 2B from the τ–p data than from the t–x data alone. This is because the horizontal slowness, p, at the intersection between the layer 2A curve and the water wave is the reciprocal of the basement velocity; and the slowness value at which the layer 2 energy dies off equates to the maximum layer 2B velocity we can image (see Fig. 4 and Supplementary Fig. 1 and 2). Additionally, the τ–p transformed data are valuable for tracing the refraction path of layer 2A which is often difficult to track behind the water wave in the t–x image. Nevertheless, the τ–p transformed data are most beneficial when used in tandem with t–x data. For example, concurrently fitting the position of the layer 2A/2B caustic in t–x adds detail to the velocity model that can be lost by fitting the τ–p times alone. Thus, the simultaneous travel time fitting in both the t–x and τ–p domains captures the main variations in upper crustal structure (i.e., average layer 2A thickness and velocity). As a trade-off, though, this method of using only P-wave events misses some of the more detailed structural information that can be found from waveform inversion (Collier and Singh, 1997; Singh et al., 1998; Hussenoeder et al., 2002a,b) or detailed AVO studies (Hussenoeder et al., 1996; Nedimović et al., 2005). However, to confirm the validity of our velocity models and phase identifications, we compared representative t–x and τ–p gathers to model gathers produced using the reflectivity method (Kennett, 1993) and found good agreement.

5.2. Averaging models

In the following section of this paper, we present the results of our modeling in terms of both along-axis variations in parameters — basement velocity, layer 2A thickness, etc. (Fig. 2, Table 1), and as average velocity models for six along-axis sections: the CLSC, nELSC,

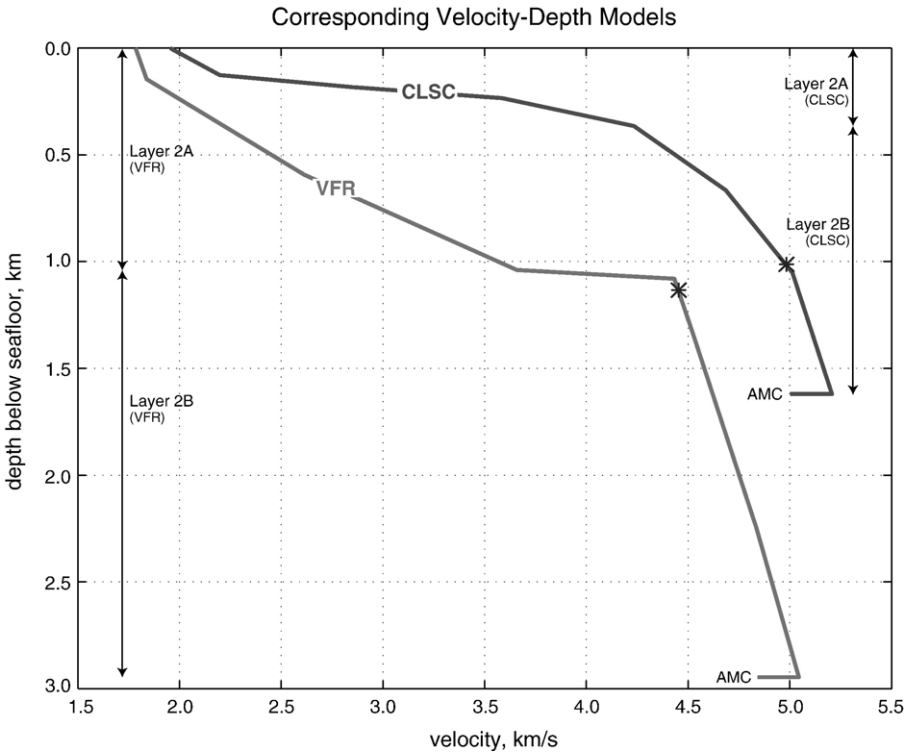

Fig. 4. Velocity–depth models corresponding to the CLSC (Fig. 3b) and VFR (Fig. 3d) travel-time curves. The dark gray stars show the maximum depth at which rays sample layer 2B for each example.

transitional ELSC, cELSC, northern VFR (nVFR), southern VFR (sVFR) (Fig. 5, Supplementary Fig. 3, Supplementary Table 1). A danger of averaging a collection of individual models is that the resulting velocity model will be smoother than the individual models and not representative of the segment (for example, lacking a well-defined transition interval at the base of layer 2A). To lessen this problem, we took advantage of the consistency in our modeling and rather than averaging the models at fixed depth intervals, averaged the nodes of our models both in velocity and in depth below the seafloor. We checked the result by taking the averaged node depths and averaging the original models in velocity at these depths. As expected, node averaging produced velocity models that more accurately preserved the character of the individual models. A caveat to the average models is that an AMC reflection is not present along all axial lines (Figs. 2 and 5, Supplementary Fig. 3), and hence the depth and velocity values of layer 2B in these areas are unconstrained. Therefore, the layer 2B values for models with no AMC reflection were not included in the average calculations.

5.3. Along-axis crustal structure

A prominent difference in upper crustal structure between the CLSC and VFR is visible in the supergather examples in Fig. 3. For the CLSC example, the layer 2A and AMC reflections have two-way travel times of 0.3 and 0.75 s below the seafloor while at the VFR these events appear 1.05 and 1.65 s below the seafloor. These changes in reflection times result primarily from an increase in layer 2A thickness and AMC depth from 0.4 to 1.0 km, and 1.5 to 2.8 km, respectively (Fig. 4, Supplementary Table 1). Along the CLSC, most of the wide-angle reflection/refraction arrivals from the thin upper crust above the AMC are captured by the MCS streamer as evidenced by the small time offset (~0.8 s) between AMC reflection and 2B refraction at the furthest offsets (Fig. 3b). However, due to the much thicker upper crust along the VFR, the data include refractions from only the upper part of layer 2B, down to ~1.2 km below the seafloor (Figs. 3d and 4). Therefore, when estimating the AMC depth by matching the arrival times of the available AMC reflections, we must assume

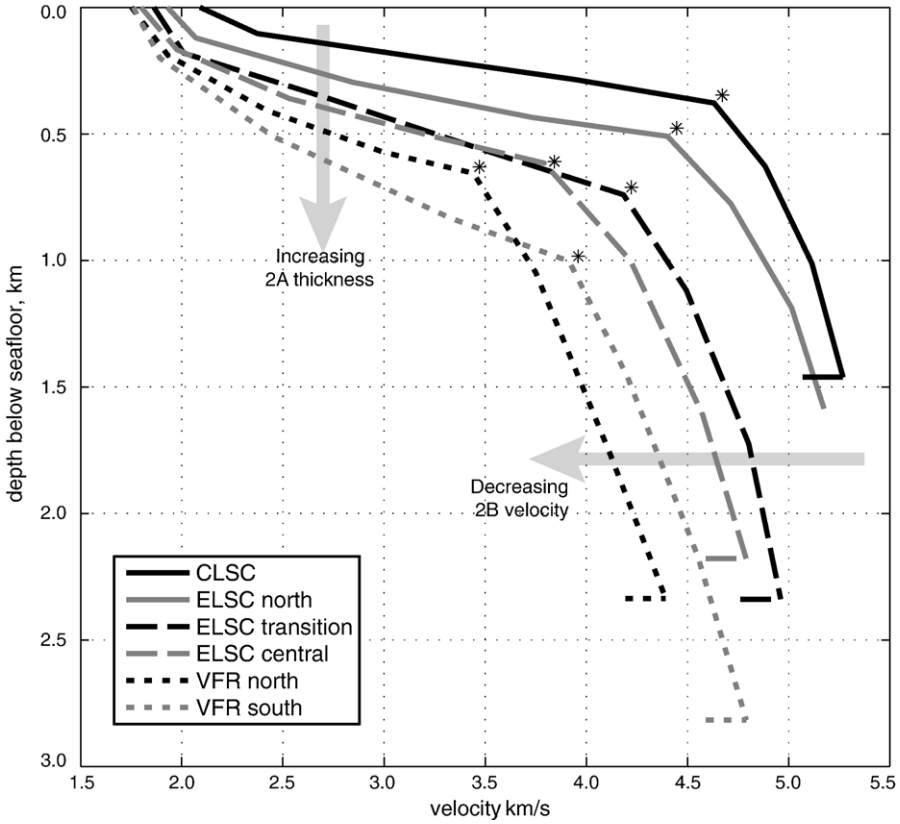

Fig. 5. Average along-axis velocity–depth models highlight the main north-to-south trends of decreasing basement and layer 2 velocities, increasing layer 2A thickness, and increasing AMC depth. The velocity gradient change marking the layer 2A/2B interface is identified by a star. Horizontal lines at the base of the model indicate the presence of an AMC.

that the lower part of layer 2B continues to have low positive velocity gradients, typical of this part of the crust. For the VFR, this assumption is supported by tomographic results that show layer 2B velocities at the spreading axis increase relatively steadily from ~4.0 to ~5.5 km/s (Turner et al., 1999), consistent with our modeling results of layer 2B. However, it is important to note that a thin low velocity zone has been found above the AMC along some spreading centers due to the local thermal structure (Singh et al., 1998). So, while the assumption of the low positive gradient is reasonable, it is not universally valid.

Another noticeable result from the velocity modeling is the variable nature of the crustal structure along both spreading systems. Showing the characteristic depth and velocity values of all 63 models, Fig. 2 illustrates the along-axis systematic changes such as southwardly increasing layer 2A thickness and AMC depth, and decreasing velocities throughout much of the crustal layers. Fig. 5 presents the average velocity models of each section, plotted together, to again demonstrate these changes. In the following text, we discuss the distinctions between each section, as well as the possible factors driving the significant along-axis variability in the basin.

6. Discussion

Compared to most oceanic spreading systems with stable accretionary processes, the dual systems of the Lau basin exhibit a wide range of along-axis upper crustal characteristics within a relatively small geographic area. Paralleling the morphologic and petrologic trends between the north and south ends of the two systems (Table 1), our results show velocity reductions as great as ~1 km/s in layer 2B and increases in layer 2 thickness of nearly 1.4 km between the CLSC and VFR (Fig. 2, Table 1). Much of this can be attributed to the petrologic changes, from MORB-like to arc-like, present in the extruded magmas as the distance between the axes and the active Tofua volcanic arc narrows (Fig. 1) (Pearce et al., 1995). However, the decreasing spreading rate along the same trend, from ~90 mm/yr along the CLSC and nELSC to ~40 mm/yr along the sVFR, may also contribute to the variability.

6.1. Central Lau Spreading Center

West of the Tofua volcanic arc by more than 160 km, geochemical studies of CLSC rock samples show typical tholeiitic MORB composition with no island arc signature (Table 1) (Hawkins et al., 1994; Hawkins, 1995; Pearce et al., 1995). Analyses by Pearce et al. (1995) and Martinez and Taylor (2002) suggest this is due to the spreading center lying beyond the inboard limit of subduction zone influences and therefore being supplied solely with the fertile mantle material coming into the basin from the west. A comparison of our modeling results with other mid-ocean ridges of MORB composition also suggests an absence of arc influence in the upper crust of the CLSC. Much like the EPR (Fig. 6a), JdFR (Fig. 6b), and a robust section of the MAR (Fig. 6a), the CLSC has an average basement velocity just above 2 km/s that increases only slightly through a ~100 m thick lower velocity layer at the top of the crust. Below this lower-velocity region, our observed layer 2A velocities are comparable to most of these ridges, while our 2B velocities show slightly slower values at 4.98 km/s versus ~5.4 km/s. However, we note that our layer 2B velocities lie closer to those of the JdFR, another intermediate-rate spreading ridge, than the fast-spreading EPR. Conversely, the layer 2A thicknesses and AMC depths of the CLSC are more similar to values seen along the EPR. Together with the geochemical findings, these upper crustal features suggest that the CLSC is undergoing spreading processes very similar to typical mid-ocean spreading centers, despite being located within a back-arc basin.

6.2. Eastern Lau Spreading Center/Valu Fa Ridge

Beginning about 60 km closer to the Tofua volcanic arc than the CLSC, the ELSC/VFR system displays most of the along-axis variability seen in the Lau basin MCS data. As seen in Table 1, the geochemical composition of the erupted magmas transition from MORB-like basalts with a slight arc signature along nELSC to basaltic andesites and rhyodacites along the VFR (Pearce et al., 1995), concurrent with the axial morphology changing from a shallow trough to a blade-like high. These characteristics may reflect changes in magma supply, decreasing spreading rate, increasing viscosity of the magmas (Jenner et al., 1987; Vallier et al., 1991), and/or increasing volatile concentration of erupted magmas, evidenced by the increasing vesicularity in rock samples (Jenner et al., 1987; Vallier et al., 1991; Pearce et al., 1995). The systematic trends seen from the seismic data (Figs. 2 and 5), especially the decreasing layer 2B velocities, correlate well with the increasing subduction influences and indicate that changes in magma chemistry and supply directly affect the upper crustal architecture. Section 6.3 further explores the mineralogical influences. Fig. 6 also displays how the average velocity model for the nELSC matches relatively well with the CLSC model, while cELSC and VFR models noticeably differ from all the spreading centers extruding MORB-like magmas.

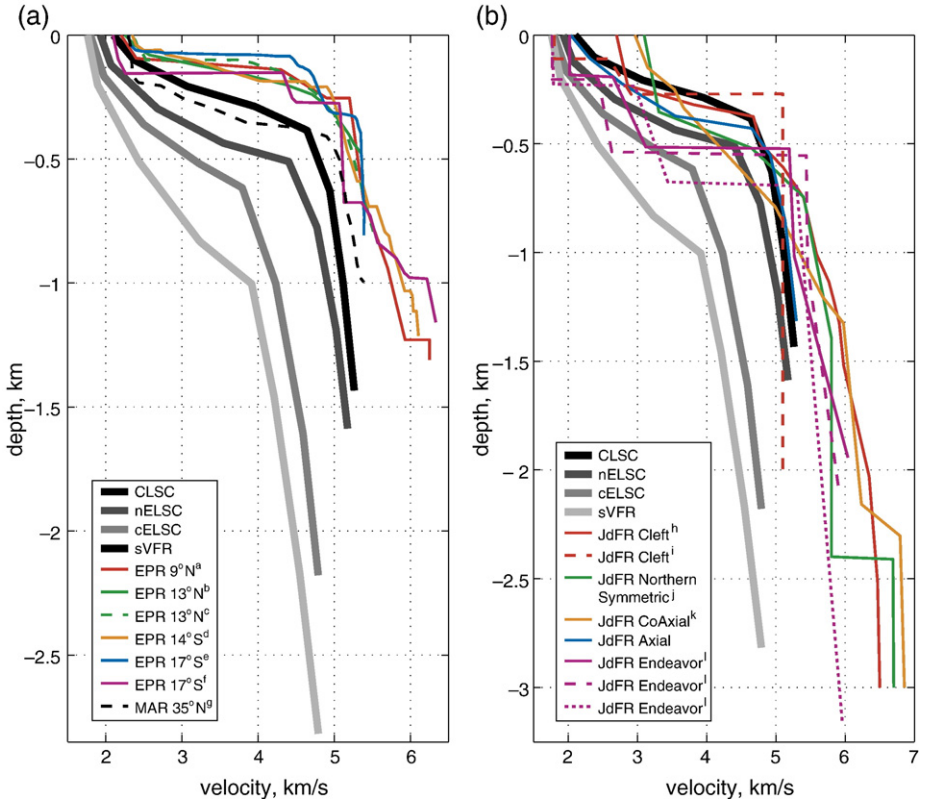

Fig. 6. (a) Velocity model comparison for the Lau basin, EPR, and a robust segment of the MAR. For the CLSC, EPR, and MAR, the basement and layer 2A velocities agree well, while the layer 2B thicknesses and AMC depths are similar. However, the EPR layer 2A is significantly thinner and its layer 2B velocities are measurably faster ([a]Vera et al., 1990, [b]Kappus et al., 1995, [c]Harding et al., 1989, [d]Tolstoy et al., 1997, [e]Hussenoeder et al., 2002b, [f]Detrick et al., 1993, [g]Hussenoeder et al., 2002a). (b) Recent studies of the Endeavor ([l]Van Ark et al., 2007) and Cleft ([i]Canales et al., 2005) segments of the Juan de Fuca Ridge show basement and upper layer 2A velocities similar to the Lau basin velocities. The cELSC has lower layer 2A velocities closer to those of the Endeavor segment, while the CLSC and nELSC more closely resembles the other JdFR segments ([j]Christeson et al., 1993, [k]Sohn et al., 1997, [h]McDonald et al., 1994). In both (a) and (b), the cELSC and VFR models clearly lie outside mid-ocean ridge velocity–depth bounds.

Unique amongst the basin's spreading centers is the intermediate-fast spreading (~77–95 mm/yr) nELSC that displays axial valley morphology, an isolated AMC reflection (Fig. 2), and a weak subduction zone influence in the erupted magmas (Table 1) (Pearce et al., 1995). It is comparable to the CLSC in spreading rate and layer 2A structure, with side-scan studies showing fairly fresh magmas along the axis (Parson et al., 1990; Taylor et al., 1996). However, due to the combination of these characteristics (Wiedicke and Habler, 1993), we propose that the nELSC is dying out as the CLSC propagates southward and suggest a reduced magma supply for the spreading section.

Between the nELSC and cELSC, the short transitional segment holds the return of the axial high morphology and relatively continuous AMC reflection previously seen along the CLSC (Fig. 2). The petrology also undergoes a noticeable shift from MORB-like with a slight arc component to strongly-depleted basalts (Jenner et al., 1987; Vallier et al., 1991; Pearce et al., 1995), indicating a possible transition to a greater subduction zone influence. This is coincident with a distinct change in basement and layer 2B velocities (Figs. 2, 5 and 6), again suggesting that there is a direct magmatic influence on crustal velocities.

Proceeding southward along the cELSC and VFR, we see increases of ~0.6 km in both layer 2A thicknesses and AMC depths and decreases in already low layer 2A and 2B velocities by as much as 0.45 km/s and 0.73 km/s, respectively (Figs. 2, 5 and 6). These trends parallel the continued petrologic transitions in the erupted lavas to more viscous, volatile-rich compositions (Jenner et al., 1987; Vallier et al., 1991; Pearce et al., 1995). Fig. 6 shows how the velocity and depth changes shifted the ELSC and VFR models outside the

velocity and depth bounds of other mid-ocean ridge models (i.e., the EPR or JdFR), especially in the layer 2B velocities, and thus how greatly the subduction zone influences the ELSC/VFR spreading systems.

6.3. Mineralogical influence on crustal velocities

Previous studies of upper crustal seismic structure have indicated that the observed velocities are dominated by porosity, the aspect ratio of cracks, and the reduction of porosity with increasing confining pressure (e.g., Christensen, 1984, 1986; Wilkens et al., 1991). With the wide range of crustal velocities seen along the Lau basin spreading axes, these factors undoubtedly control the structure of our individual velocity profiles, as well. However, it is conceivable that the velocity variations between the different ridge sections, particularly in the lower porosity layer 2B, are due to the lava chemistry and resulting mineralogical differences.

To assess the velocity contrast resulting solely from the MORB-versus-arc difference in chemistries, we calculated predicted velocities for the near-axis samples in the Petrological Database of the Ocean Floor (PETDB). These predictions were generated from the full mineralogical assemblage of the sample as determined by the Cross-Iddings-Pirsson-Washington (CIPW) norm (e.g., White and McKenzie, 1989; Korenaga et al., 2002) or directly from the weight percentages of SiO_2, MgO and CaO in the sample using the empirical formula of Behn and Kelemen (2003) (examples in Supplementary Table 2). For the CIPW-based approach, relevant mineral velocities were taken from Sobolev and Babeyko (1994) and the sample velocity was calculated as the average of the Hashin–Shtrikman bounds on the assemblage (e.g., Behn and Kelemen, 2003). Although the two approaches predicted different sample velocities with the values from Behn and Kelemen (2003) consistently being higher, the differences in velocities between samples were nearly the same, thus suggesting that the latter is robust and reliable.

We observed a correlation between slightly decreasing velocities and increasing proximity to the volcanic arc by plotting the calculated sample velocities as a function of sample latitude (Fig. 7). The differences in average velocity between the samples from the nELSC

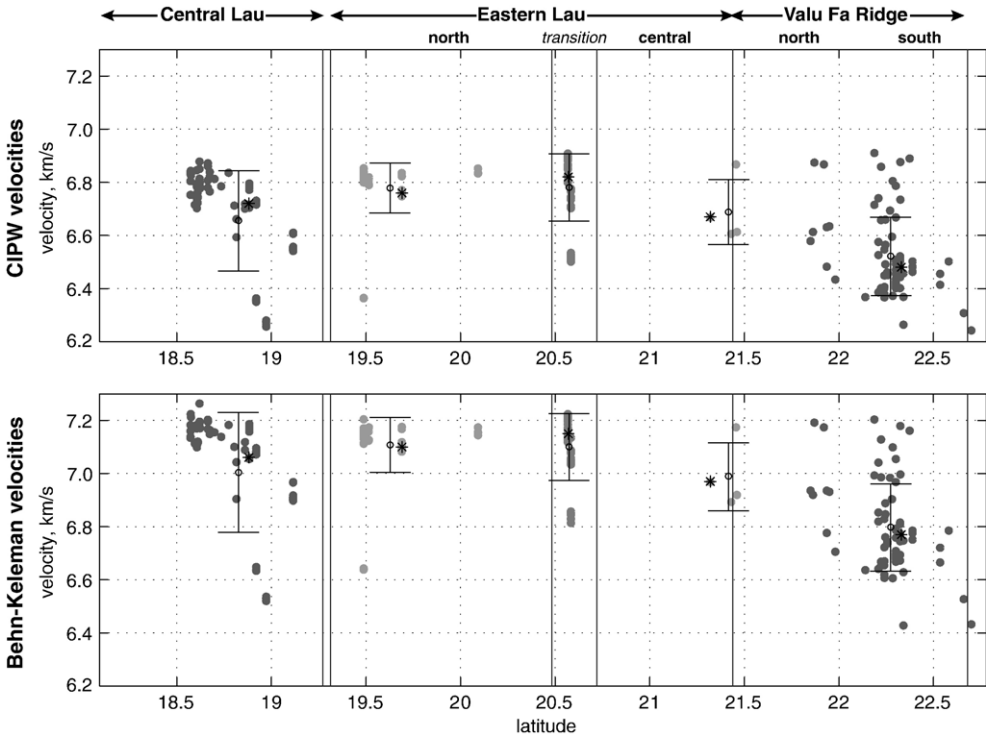

Fig. 7. Calculated velocities based on mineralogy. Top and middle panels plot CIPW-derived velocities and Behn–Keleman-derived velocities, respectively, versus latitude. Mean values for each section are shown by error bars representing one standard deviation. Stars denote samples looked at in detail in Supplementary Table 2.

and VFR and the CLSC and VFR was 0.29 km/s and 0.17 km/s, respectively. Similarly, the difference in velocities between actual samples representative of the nELSC (19.69°S Pearce et al., 1995), the VFR (22.33°S Vallier et al., 1991) and the CLSC (18.88°S Pearce et al., 1995), is 0.28–0.33 km/s (Supplementary Table 2). Thus, while mineralogical changes can explain nearly a half of the approximately 0.6 km/s decrease in the average layer 2B velocity, it is unlikely that they are the sole cause. We infer that the unusually low velocities seen along the VFR, and to a lesser extent along the cELSC, result from a combination of mineralogy and increased intrinsic porosity. The increased porosity is, in turn, likely a reflection of the progressively more important role volatiles play in the eruption process as the distance to the arc decreases southward. Evidence for this comes from samples dredged along the VFR which are consistently highly vesiculated (Jenner et al., 1987; von Stackelberg, 1988) and elevated water content relative to MORB: 0.6–1.8 wt.% H_2O for the samples of (Sunkel, 1990).

6.4. Layer 2A thickness versus AMC depth

Another aspect of the along-axis structure that distinguishes the Lau basin results from typical mid-ocean spreading centers is the ratio of layer 2A thickness to AMC depth, or '*R*-value' (Buck et al., 1997; Blacic et al., 2004; Canales et al., 2005) (Fig. 8). The available measurements of this ratio for mid-ocean ridge settings typically yield values lying roughly in the range 0.13–0.2. In contrast, our results for the cELSC, nVFR, and sVFR (calculated from values listed in Table 1) define a trend line that is considerably steeper with a maximum *R*-value along the sVFR of 0.35.

To explain the observed *R*-values, Buck et al. (1997) formulated a set of simple models based on a force balance between the pressure on the magma chamber and

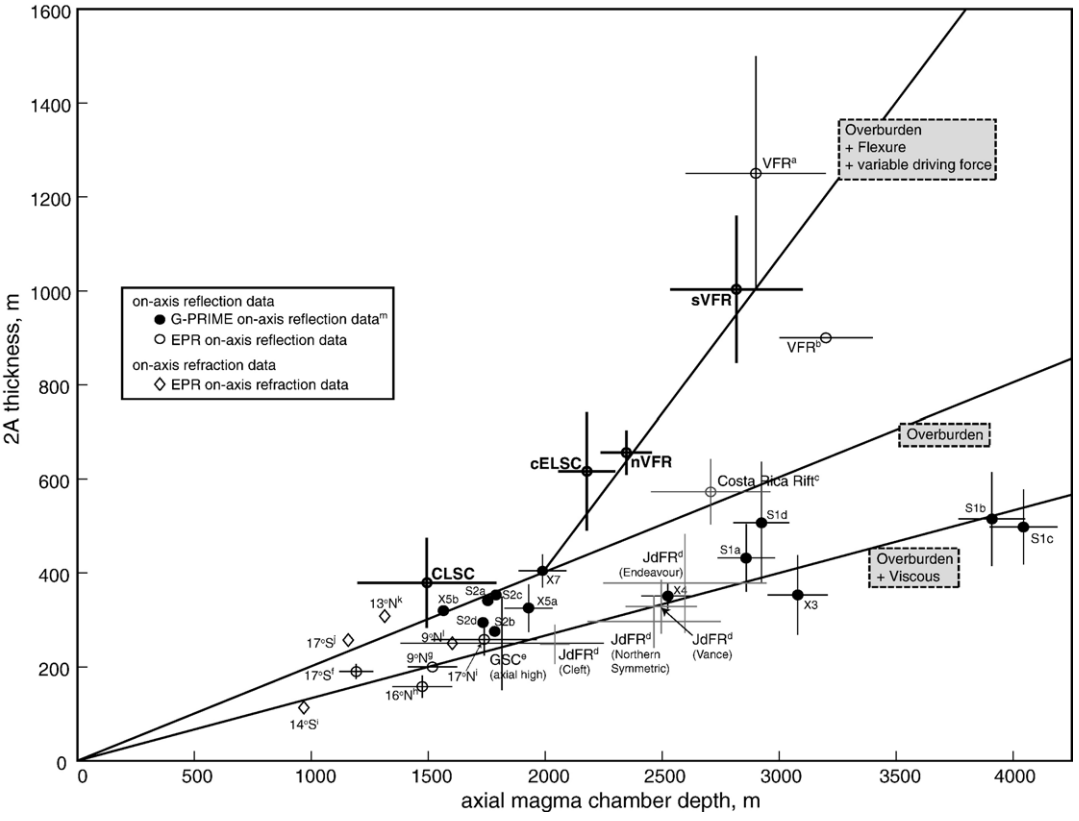

Fig. 8. Layer 2A thickness versus AMC depth, updated from Buck et al. (1997). The steeper trend of the ELSC/VFR spreading sections indicates that they are influenced by overburden plus flexural and/or another variable driving force. With the exception of the CLSC, the Lau basin ratios are measurably different from most other mid-ocean spreading systems. ([a]Turner et al., 1999, [b]Collier and Sinha, 1992, [c]Mutter, 1995, [d]Carbotte et al., 2006, [e]Detrick et al., 2002, [f]Mutter et al., 1995a, [g]Harding et al., 1993, [h]Carbotte et al., 1996, [i]Mutter et al., 1995b, [j]Detrick et al., 1993, [k]Harding et al., 1989, [l]Vera et al., 1990, [m]Blacic et al., 2004).

the pressure required to drive magma up through a dike to the surface. They assumed that the thickness of layer 2A, taken as a proxy for the extrusive section, would grow until the pressure balance was achieved. In the simplest model, the weight of the erupting magma column was balanced against the overburden pressure on the magma chamber. A slight elaboration of this basic model allows for a dynamic pressure gradient to overcome the viscous drag associated with magma flow in a dike. With suitable choices for density and dynamic pressure gradient, these models predict constant *R*-values of 0.2 and 0.13, respectively. While most of the then-available data are adequately explained by the models, the ratio for the VFR, with its deeper magma chamber (Turner et al., 1999) was not. This prompted Buck et al. (1997) to suggest that there was an overpressure associated with deeper magma chambers, caused by the flexural resistance of a stronger upper crust to buoyant uplift from a mantle source. However, more recent measurements from the Galapagos Spreading Center (Blacic et al., 2004) and Juan de Fuca Ridge (Van Ark et al., 2007), both of which are spreading at intermediate rates, show that increased *R*-values are not necessarily observed in mid-ocean ridge environments even when magma chamber depths exceed 2000 m (Fig. 8).

In light of these recent results for mid-ocean ridges, we were prompted to find a more specifically back-arc basin-based mechanism to explain the range of *R*-values observed in the Lau basin. Relative to other mid-ocean ridge measurements, the *R*-value for CLSC is only slightly elevated. However, south of the transitional segment where the subduction zone influence becomes progressively more prominent, layer 2A thicknesses increase rapidly, concurrently elevating the *R*-values. We propose that the presence of volatiles in the magma causes this increased thickness since the density of magma is strongly pressure dependent once volatile

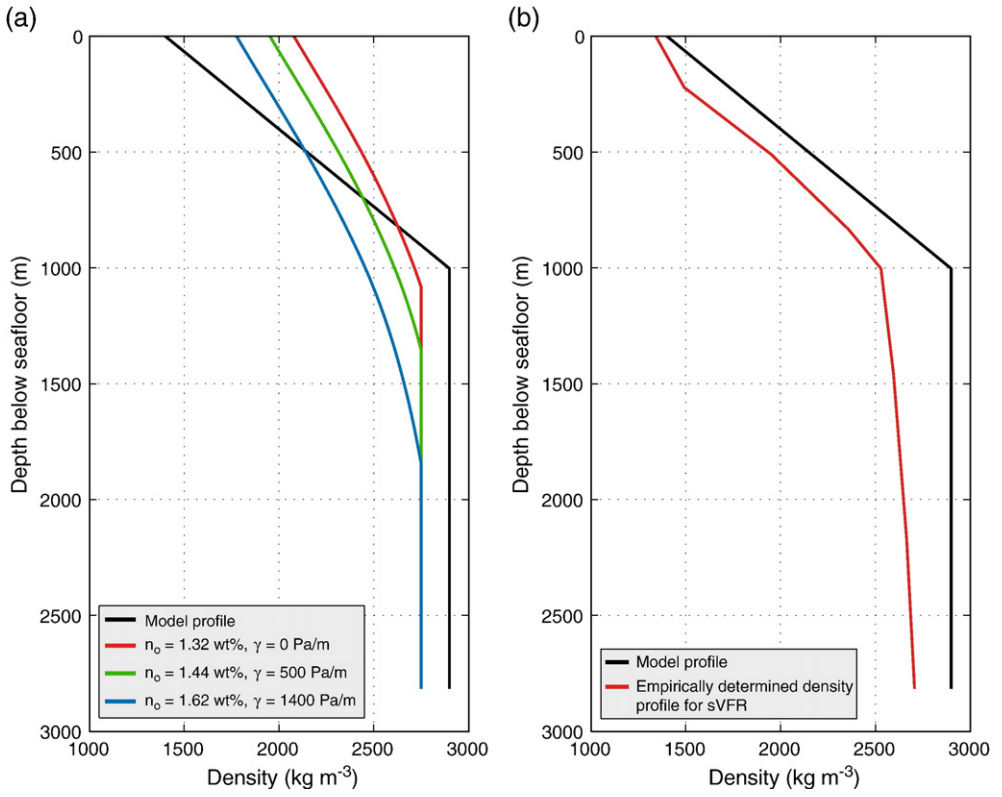

Fig. 9. (a) Density profiles of the upper crust model and corresponding magma columns that satisfy overall force balance for different volatile concentrations, n_o, and viscous pressure gradients, γ. The layer 2A thickness and magma chamber depth are taken from the average sVFR results (Table 1). The densities of the intrusive section and unsaturated magma are 2900 and 2750 kg m^{-3}, respectively, identical to Buck et al. (1997). However, the densities within the extrusive section are not constant but increase linearly with depth since this is a better match to the seismic results and ensures a physically reasonable solution. The higher water concentrations saturate deeper and can overcome greater viscous head loss. (b) Density profile for the average sVFR model computed using the empirical relation of Carlson and Herrick (1990) compared to the model upper crustal density profile used the calculations (a).

saturation is reached (e.g., Bower and Woods, 1997). We checked the viability of this mechanism by calculating the water content needed to reproduce the ELSC/VFR measurements (Table 1). In these calculations, we again balance the weight of the magma chamber column against the overburden pressure, with or without the dynamic pressure head loss. The difference being that we follow the approach of Bower and Woods (1997) to calculate the density profile of the magma column assuming that water is the sole volatile. Exsolution of water occurs once the concentration exceeds the saturation weight fraction, n_s, which is related to pressure, p, by a form of Henry's Law, $n_s = sp^{1/2}$. An appropriate value for the solubility constant, s, depends on both the composition of the magma and the mix of volatiles if, for example, CO_2 were present, the solubility of water would be lowered. Since a reasonable range of s values is $2–4\times10^{-6}$ $Pa^{-1/2}$ (e.g., Burnham, 1975; Sparks and Pinkerton, 1978), we chose a value at the lower end because it corresponds to a water saturation of ~2 wt.% at the depth of the magma lens along the ELSC/VFR. This percentage is an appropriate upper bound based on water concentrations observed in glass samples from the VFR (Sunkel, 1990). However, although the value of the solubility constant affects the details of the calculation, we find that the presence of volatiles can drive the creation of a thicker extrusive section provided the concentration reaches saturation before or during eruption.

Using the above assumptions and conditions, density profiles for magma and upper crust that approximate the sVFR are shown in Fig. 9a for different values of the viscous pressure gradient. Although we kept the same average densities for the extrusive and intrusive section as Buck et al. (1997), we have approximated the density profile through layer 2A by a linear gradient. This is a better fit to the density profile one would predict from the seismic results (Fig. 9b) and is necessary to ensure that the solution is physically reasonable with magma density exceeding basement density at the seafloor. Including a viscous pressure loss requires a higher volatile concentration in the magma and a deeper saturation depth, thus predicted water concentrations increase from 1.3 to 1.5 wt.% and saturation depths from 1.1 to 1.3 km if the viscous pressure gradient is set to 1400 Pa/m (Fig. 9a). An appropriate gradient is hard to estimate and can be expected to increase towards the seafloor due to volatile loss (Shaw, 1972). The morphologic evolution of the axes from rounded-high along the cELSC to blade-like structure along the VFR, coupled with the change to more andesitic magmas suggests the increased importance of viscosity for the VFR (Wiedicke and Collier, 1993). These factors and the deepening of the magma chamber southwards from the cELSC to sVFR are consistent with increased volatile concentration as the distance to the arc decreases.

Although many relevant parameters remain unknown, the presence of volatiles appears to be a plausible explanation for the thicker layer 2A seen along the ELSC/VFR. As noted earlier, the velocity structure along these segments is consistent with increased porosity throughout the upper crust, and the highly vesicular rocks dredged from the VFR indicate a significant volatile presence (Jenner et al., 1987; von Stackelberg et al., 1988). Additionally, the estimated reflection coefficient from the top of the magma chamber is unusually high along some parts of the VFR suggesting that the magma chamber could be oversaturated in volatiles. However, the reflection amplitudes are not so high that other causes, such as tuning from a layered magma chamber, can be excluded (Collier and Sinha, 1992).

7. Conclusion

The Lau basin MCS data reveals large along-axis variation in the upper crustal structure of the CLSC and ELSC/VFR. From velocity–depth modeling, we find that the CLSC has average layer 2 thicknesses and velocities comparable to intermediate and fast spreading mid-ocean ridges (Figs. 6 and 8). These results correlate well with the broad axial high morphology (Taylor et al., 1996) and MORB-like petrology (Pearce et al., 1995) previously noted along this system. The ELSC/VFR is more unusual in that it exhibits along-axis changes in morphology, petrology, and crustal structure that are indicative of a systematic increase in subduction zone influence. The morphologic transition from a shallow axial valley along the nELSC to axial high along cELSC coincides with the return of a nearly continuous AMC reflector, decreasing crustal velocities, increasing layer 2A thickness, and rock samples of increasingly depleted basaltic composition (Pearce et al., 1995). At the southern transition from the cELSC to the VFR, the axial high becomes a steep, blade-like axial high. This transition correlates with a continued decrease in crustal velocities along the nVFR (1.75 km/s basement, 2.51 km/s average layer 2A, 3.93 km/s average layer 2B), a thickening of layer 2 to more than 2.5 km along the sVFR, and an overall petrologic transition to basaltic andesites and rhyodacites (Pearce et al., 1995). From the morphologic and petrologic data, models of the Lau basin (Pearce et al., 1995; Martinez and Taylor, 2002), and our calculations pertaining to the mineralogical influence on velocities and layer thicknesses, we interpret the variability in crustal structure along the

CLSC and ELSC/VFR systems to be due to the increasing influences of the Tonga subduction zone through the increase of volatiles within the magmas. Primarily along the ELSC/VFR, the geochemical changes that occur as the axis nears the active volcanic arc show an increasing amount of volatiles in what could be normal MORBs. This in turn enhances the viscosity, porosity, and fracturing of material being supplied to the ridge. We think that these effects could be occurring in both the intruded and extruded material, thus accounting for the thick crustal layers and low crustal velocities.

Acknowledgements

We would like to thank the captain and crew of the R/V Maurice Ewing for their help and support during this Lau Basin cruise. Additionally, a thank you goes to Paul Henkart and the Scripps Industrial Associates for the use of the SIOSEIS processing package. This paper greatly benefitted from the helpful comments and suggestions of Brian Taylor, Debi Kilb, and our reviewer, Jenny Collier. This study was carried out under grants OCE-9529870 and OCE-0002600.

Appendix A. Supplementary data

Supplementary data associated with this article can be found, in the online version, at doi:10.1016/j.epsl.2007.04.021.

References

Baran, J.M., Cochran, J.R., Carbotte, S.M., Nedimoviæ, M.R., 2005. Variations in upper crustal structure due to variable mantle temperature along the Southeast Indian Ridge. Geochem. Geophys. Geosys. 6. doi:10.1029/2005GC000943.

Behn, M.D., Kelemen, P.B., 2003. Relationship between seismic P-wave velocity and the composition of anhydrous igneous and meta-igneous rocks. Geochem. Geophys. Geosys. 4. doi:10.1029/2002GC000393.

Blacic, T.M., Ito, G., Canales, J.P., Detrick, R.S., Sinton, J., 2004. Constructing the crust along the Galapagos Spreading Center 91.3°–95.5°W: correlation of seismic layer 2A with axial magma lens and topographic characteristics. J. Geophys. Res. 109. doi:10.1029/2004JB003066.

Boespflug, X., Dosso, L., Bougault, H., Joron, J.L., 1990. Trace element and isotopic (Sr, Nd) geochemistry of volcanic rocks from the Lau Basin. Geol. Jahrb. 92, 503–516.

Bower, S.M., Woods, A.W., 1997. Control of magma volatile content and chamber depth on the mass erupted during explosive volcanic eruptions. J. Geophys. Res. 102, 10273–10290.

Burnham, C.W., 1975. Water and magmas—mixing model. Geochim. Cosmochim. Acta 39, 1077–1084.

Buck, W.R., Carbotte, S.M., Mutter, C., 1997. Controls on extrusion at mid-ocean ridges. Geology 25, 935–938.

Canales, J.P., Ito, G., Detrick, R.S., Sinton, J., 2002. Crustal thickness along the western Galapagos Spreading Center and the compensation of the Galapagos hotspot swell. Earth Planet. Sci. Lett. 203, 311–327.

Canales, J.P., Detrick, R.S., Carbotte, S.M., Kent, G.M., Diebold, J.B., Harding, A.J., Babcock, J.M., Nedimoviæ, M.R., Van Ark, E., 2005. Upper crustal structure and axial topography at intermediate spreading ridges: seismic constraints from the southern Juan de Fuca Ridge. J. Geophys. Res. 110. doi:10.1029/2005JB003630.

Carbotte, S.M., Mutter, C.Z., Mutter, J.C., Speigelman, M., Correa, G., McNutt, M., Bhat, V., Cruz-Orozco, R., 1996. Influence of spreading rate and magma supply on crustal magma bodies: results from a recent seismic study of the shallow East Pacific Rise north of the Orozco transform fault. RIDGE Events 7, 1–4.

Carbotte, S.M., Detrick, R.S., Harding, A., Canales, J.P., Babcock, J., Kent, G., Van Ark, E., Nedimoviæ, M., Diebold, J., 2006. Rift topography linked to magmatism at the intermediate spreading Juan de Fuca. Geology 34, 209–212.

Carlson, R.L., 1998. Seismic velocities in the uppermost oceanic crust: age dependence and the fate of layer 2A. J. Geophys. Res. 103, 7069–7077.

Carlson, R.L., Herrick, C.N., 1990. Densities and porosities in the oceanic crust and their variations with depth and age. J. Geophys. Res. 95, 9153–9170.

Chen, Y.S.J., Lin, J., 2004. High sensitivity of ocean ridge thermal structure to changes in magma supply: the Galapagos Spreading Center. Earth Planet. Sci. Lett. 221, 263–273.

Christensen, N.I., 1984. Pore pressure and oceanic crustal seismic structure. Geophys. J. R. Astr. Soc. 79, 411–423.

Christensen, N.I., 1986. The influence of pore pressure on oceanic crustal seismic velocities. J. Geodyn. 5, 45–48.

Christeson, G.L., Purdy, G.M., Rohr, K.M.M., 1993. Structure of the northern symmetrical segment of the Juan de Fuca Ridge. Mar. Geophys. Res. 15, 219–240.

Christeson, G.L., McIntosh, K.D., Karson, J.A., 2007. Inconsistent correlation of seismic layer 2a and lava layer thickness in oceanic crust. Nature 445. doi:10.1038/nature05517.

Collier, J., Sinha, M., 1990. Seismic images of a magma chamber beneath the Lau Basin back-arc spreading centre. Nature 346, 646–648.

Collier, J.S., Sinha, M.C., 1992. Seismic mapping of a magma chamber beneath the Valu Fa Ridge, Lau Basin. J. Geophys. Res. 97, 14031–14053.

Collier, J.S., Singh, S.C., 1997. Detailed structure of the top of the melt body beneath the East Pacific Rise at 9 degrees 40'N from waveform inversion of seismic reflection data. J. Geophys. Res. 102, 20287–20304.

Detrick, R.S., Harding, A.J., Kent, G.M., Orcutt, J.A., Mutter, J.C., Buhl, P., 1993. Seismic structure of the southern East Pacific Rise. Science 259, 499–503.

Detrick, R.S., Needham, H.D., Renard, V., 1995. Gravity anomalies and crustal thickness variations along the Mid-Atlantic Ridge between 33°N and 40°N. J. Geophys. Res. 100, 3767–3787.

Detrick, R.S., Sinton, J.M., Ito, G., Canales, J.P., Behn, M., Blacic, T., Cushman, B., Dixon, J.E., Graham, D.W., Mahoney, J.J., 2002. Correlated geophysical, geochemical, and volcanological manifestations of plume-ridge interactions along the Galapagos Spreading Center. Geochem. Geophys. Geosys. 3. doi:10.1029/2002GC000050.

Diebold, J.B., Stoffa, P.L., 1981. The travel-time equation, tau-*p* mapping, and inversion of common midpoint data. Geophysics 46, 238–254.

Harding, A.J., Orcutt, J.A., Kappus, M.E., Vera, E.E., Mutter, J.C., Buhl, P., Detrick, R.S., Brocher, T.M., 1989. Structure of young oceanic-crust at 13°N on the East Pacific Rise from expanding spread profiles. J. Geophys. Res. 94, 12163–12196.

Harding, A.J., Kent, G.M., Orcutt, J.A., 1993. A multichannel seismic investigation of upper crustal structure at 9°N on the East Pacific Rise — implications for crustal accretion. J. Geophys. Res. 98, 13925–13944.

Hawkins, J.W., 1995. The geology of the Lau Basin. In: Taylor, B. (Ed.), Backarc Basins: Tectonics and Magmatism. Plenum Press, New York, pp. 63–138.

Hawkins, J.W., Parson, L.M., Allan, J.F., 1994. Introduction to the scientific results of Leg 135: Lau Basin–Tonga Ridge drilling transect. In: Hawkins, J.W., Parson, L.M., Allan, J. (Eds.), Proceedings of the Ocean Drilling Program Leg 135, Scientific Results. Ocean Drilling Program, College Station, TX, pp. 3–5.

Hooft, E.E.E., Schouten, H., Detrick, R.S., 1996. Constraining crustal emplacement processes from the variation in seismic layer 2A thickness at the East Pacific Rise. Earth Planet. Sci. Lett. 142, 289–309.

Hussenoeder, S.A., Collins, J.A., Kent, G.M., Detrick, R.S., Harding, A.J., Orcutt, J.A., Mutter, J.C., Buhl, P., 1996. Seismic analysis of the axial magma chamber reflector along the southern East Pacific Rise from conventional reflection profiling. J. Geophys. Res. 101, 22087–22105.

Hussenoeder, S.A., Kent, G.M., Detrick, R.S., 2002a. Upper crustal seismic structure of the slow spreading Mid-Atlantic Ridge, 35°N; constraints on volcanic emplacement processes. J. Geophys. Res. 107. doi:10.1029/2001JB001691.

Hussenoeder, S.A., Detrick, R.S., Kent, G.M., Schouten, H., Harding, A.J., 2002b. Fine-scale seismic structure of young upper crust at 17°20'S on the fast spreading East Pacific Rise. J. Geophys. Res. 107. doi:10.1029/2001JB001688.

Jenner, G.A., Cawood, P.A., Rautensclein, M., White, W.M., 1987. Composition of back-arc volcanics Valu Fa Ridge, Lau Basin: evidence for a slab derived component in their mantle source. In: Weaver, S.D., Johnson, R.W. (Eds.), Tectonic Controls on Magma Genesis. J. Volc. and Geothermal Res., vol. 32, pp. 209–222.

Kappus, M.E., Harding, A.J., Orcutt, J.A., 1995. A base-line for upper crustal velocity variations along the East Pacific Rise at 13°N. J. Geophys. Res. 100, 6143–6161.

Kennett, B.L.N., 1983. Seismic Wave Propagation in Stratified Media. Cambridge University Press, Cambridge.

Kent, G.M., Harding, A.J., Orcutt, J.A., Detrick, R.S., Mutter, J.C., Buhl, P., 1994. Uniform accretion of oceanic-crust south of the Garrett Transform at 14°15'S on the East Pacific Rise. J. Geophys. Res. 99, 9097–9116.

Korenaga, J., Kelemen, P.B., Holbrook, W.S., 2002. Methods for resolving the origin of large igneous provinces from crustal seismology. J. Geophys. Res. 107. doi:10.1029/2001JB001030.

Martinez, F., Taylor, B., 2002. Mantle wedge control on back-arc crustal accretion. Nature 416, 417–420.

Martinez, F., Taylor, B., Baker, E.T., Resing, J.A., Walker, S.L., 2006. Opposing trends in crustal thickness and spreading rate along the back-arc Eastern Lau Spreading Center: implications for controls on ridge morphology, faulting, and hydrothermal activity. Earth Planet. Sci. Lett. 245, 655–672.

McDonald, M.A., Webb, S.C., Hildebrand, J.A., Cornuelle, B.D., Fox, C.G., 1994. Seismic structure and anisotropy of the Juan de Fuca Ridge at 45°N. J. Geophys. Res. 99, 4857–4873.

Morgan, J.P., Chen, Y.J., 1993. Dependence of ridge-axis morphology on magma supply and spreading rate. Nature 364, 706–708.

Morton, J.L., Sleep, N.H., 1985. Geology and offshore resources of Pacific Island Arc–Tonga region. In: Scholl, D.W., Vallier, T.L. (Eds.), Geology and offshore resources of Pacific island arcs–Tonga region, Circum-Pacific Council for Energy and Mineral Resources. . Earth Science Series, vol. 2. Circum Pacific Council for Energy and Mineral Resources, Houston, TX, pp. 441–453.

Mutter, C.Z., 1995. Seismic and hydrosweep study of the Western Costa Rica Rift. Eos, Trans. Am. Geophys. Union 76, 595.

Mutter, J.C., Carbotte, S.M., Su, W., Xu, L., Buhl, P., Detrick, R.S., Kent, G.M., Orcutt, J.A., Harding, A.J., 1995a. Seismic images of active magma systems beneath the East Pacific Rise between 17°05' and 17°35'S. Science 268, 391–395.

Mutter, J.C., Cormier, M.H., Wang, L., Buhl, P., Detrick, R.S., Kent, G.M., Orcutt, J.A., Harding, A., 1995b. Asymmetric crustal structure of the East Pacific Rise at 14 15'S from expanded spread profiles. Eos, Trans. Am. Geophys. Union 76, 274–275.

Nedimoviæ, M.R., Carbotte, S.M., Harding, A.J., Detrick, R.S., Canales, J.P., Diebold, J.B., Kent, G.M., Tischer, M., Babcock, J.M., 2005. Frozen magma lenses below the oceanic crust. Nature 436, 1149–1152.

Parson, L.M., Hawkins, J.W., 1994. Two-stage ridge propagation and the geological history of the Lau Backarc Basin. In: Hawkins, J.W., Parson, L.M., Allan, J. (Eds.), Proceedings of the Ocean Drilling Program Leg 135, Scientific Results. Ocean Drilling Program, College Station, TX, pp. 819–828.

Parson, L.M., Wright, I.C., 1996. The Lau-Havre-Taupo back-arc basin: a southward-propagating, multi-stage evolution from rifting to spreading. Tectonophysics 263, 1–22.

Parson, L.M., Pearce, J.A., Murton, B.J., Hodkinson, R.A., 1990. Role of ridge jumps and ridge propagation in the tectonic evolution of the Lau back-arc basin, southwest Pacific. Geology 18, 470–473.

Pearce, J.A., Ernewein, M., Bloomer, S.H., Parson, L.M., Murton, B. J., Johnson, L.E., 1995. Geochemistry of Lau Basin volcanic rocks: influence of ridge segmentation and arc proximity. In: Smellie, J.L. (Ed.), Volcanism Associated With Extension at Consuming Plate Margins. Special Publication, vol. 81. Geological Society, London, pp. 53–75.

Shaw, H., 1972. Viscosities of magmatic silicate liquids: an empirical method of prediction. Am. J. Sci. 272, 870–893.

Singh, S.C., Kent, G.M., Collier, J.S., Harding, A.J., Orcutt, J.A., 1998. Melt to mush variations in crustal magma properties along the ridge crest at the southern East Pacific Rise. Nature 394, 874–878.

Singh, S.C., Crawford, W.C., Carton, H., Seher, T., Combier, V., Cannat, M., Canales, J.P., Düsünür, D., Escartin, J., Miranda, J.M., 2006. Discovery of a magma chamber and faults beneath a Mid-Atlantic Ridge hydrothermal field. Nature 442, 1029–1032.

Sobolev, S., Babeyko, A., 1994. Modeling of mineralogical composition, density and elastic wave velocities in anhydrous magmatic rocks. Surv. Geophys. 15, 515–544.

Sohn, R.A., Webb, S.C., Hildebrand, J.A., Cornuelle, B.D., 1997. Three-dimensional tomography velocity structure of upper crust, CoAxial segment, Juan de Fuca Ridge; implications for on-axis evolution and hydrothermal circulation. J. Geophys. Res. 102, 17679–17695.

Sparks, R.S.J., Pinkerton, H., 1978. Effects of degassing on rheology of basaltic lava. Nature 276, 385–386.

Sunkel, G., 1990. Origin of petrology and geochemistry of submarine lavas from the Lau Basin (SW Pacific). Mar. Min. 9, 205–234.

Taylor, B., Zellmer, K., Martintez, F., Goodliffe, A., 1996. Sea-floor spreading in the Lau back-arc basin. Earth Planet. Sci. Lett. 144, 35–40.

Tolstoy, M., Harding, A.J., Orcutt, J.A., Detrick, R.S., Kent, G.M., Mutter, J.C., Buhl, P., 1997. Deepening of the axial magma chamber on the southern East Pacific Rise toward the Garrett Fracture Zone. J. Geophys. Res. 102, 3097–3108.

Turner, I.A., Peirce, C., Sinha, M.C., 1999. Seismic imaging of the axial region of the Valu Fa Ridge, Lau Basin—the accretionary processes of an intermediate back-arc spreading ridge. Geophys. J. Int. 138, 495–519.

Vallier, T.L., Jenner, G.A., Frey, F.A., Gill, J.B., Davis, A.S., Volpe, A. M., Hawkins, J.W., Morris, J.D., Cawood, P.A., Morton, J.L., Scholl, D.W., Rautenschlein, M., White, W.M., Williams, R.W., Stevenson, A.J., White, L.D., 1991. Subalkaline andesite from Valu Fa Ridge, a back-arc spreading center in southern Lau Basin: petrogenesis, comparative chemistry, and tectonic implications. Chem. Geol. 91, 227–256.

Van Ark, E.M., Detrick, R.S., Canales, J.P., Carbotte, S.M., Harding, A.J., Kent, G.M., Nedimoviæ, M.R., Wilcock, W.S.D., Diebold, J.B., Babcock, J.M., 2007. Seismic structure of the Endeavour Segment, Juan de Fuca Ridge: correlations with seismicity and hydrothermal activity. J. Geophys. Res. 112. doi:10.1029/2005JB004210.

Vera, E.E., Mutter, J.C., Buhl, P., Orcutt, J.A., Harding, A.J., Kappus, M.E., Detrick, R.S., Brocher, T.M., 1990. The structure of 0-My to 0.2-My old oceanic-crust at 9°N on the East Pacific Rise from expanded spread profiles. J. Geophys. Res. 95, 15529–15556.

von Stackelberg, U., P. The Shipboard Scientific, 1988. Active hydrothermalism in the Lau Back-Arc Basin (SW-Pacific): first results from the SONNE 48 Cruise (1987), Mar. Min. 7, 431–442.

White, R.S., 1979. Oceanic upper crustal structure from variable angle seismic reflection–refraction profiles. Geophys. J. R. Astron. Soc. 57, 683–726.

White, R., McKenzie, D., 1989. Magmatism at rift zones: the generation of volcanic continental margins and flood basalts. J. Geophys. Res. 94, 7685–7729.

Wiedicke, M., Collier, J., 1993. Morphology of the Valu Fa spreading ridge in the Lau Basin back-arc spreading centre. J. Geophys. Res. 98, 11769–11782.

Wiedicke, M., Habler, W., 1993. Morphotectonic characteristics of a propagating spreading system in the northern Lau Basin. J. Geophys. Res. 98, 11783–11797.

Wilkens, R.H., Fryer, G.J., Karsten, J.L., 1991. Evolution of porosity and seismic structure of upper oceanic crust: importance of aspect ratios. J. Geophys. Res. 96, 17981–17995.

Zellmer, K.E., Taylor, B., 2001. A three-plate kinematic model for Lau Basin opening. Geochem. Geophys. Geosys. 2 (Paper number 2000GC000106).